ACS APPLIED MATERIALS & INTERFACES

Research Article

www.acsami.org

Controllable Fabrication of Zinc Borate Hierarchical Nanostructure on Brucite Surface for Enhanced Mechanical Properties and Flame Retardant Behaviors

Xuesong Wang, Hongchang Pang, Wendan Chen, Yuan Lin, Lishuai Zong, and Guiling Ning*

Faculty of Chemical, Environmental & Biological Science and Technology, Dalian University of Technology, Dalian 116024, China

Supporting Information

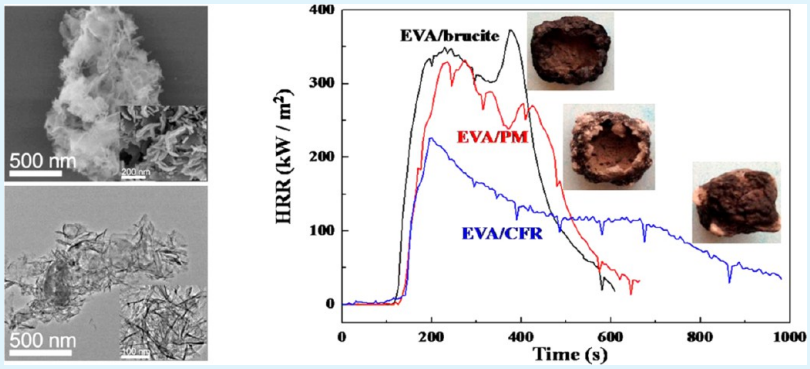

ABSTRACT: A novel and efficient halogen-free composite flame retardant (CFR) consisting of a brucite core and a fine zinc borate [$Zn_6O(OH)(BO_3)_3$] hierarchical nanostructure shell was designed and synthesized via a facile nanoengineering route. It had been demonstrated that this unique hybrid structure possessed a high BET specific surface area (65 m^2/g) and could significantly enhance the interfacial interaction when mixing with ethylene-vinyl acetate (EVA). This improved the transfer of stress between CFR particles and EVA matrix and increased the viscosity of EVA/EVA blends, which was beneficial for droplet inhibition and char forming. The mechanical properties and flammability behaviors of the EVA/CFR blends had been compared with the EVA/physical mixture (PM, with the given proportion of brucite and $Zn_6O(OH)(BO_3)_3$). The mechanical properties of EVA/CFR blends, especially the tensile strength (TS), presented a remarkable increase reaching at least a 20% increment. Meanwhile, with the same 45 wt % of fillers, the EVA/CFR formulation could achieve a limiting oxygen index (LOI) value of 33 (37.5 % higher than that of EVA/PM blends) and UL-94 V-0 rating. Moreover, the heat release rate (HRR), peak heat release rate (PHRR), total heat released (THR), smoke production rate (SPR) and mass loss rate (MLR) were considerably reduced, especially PHRR and SPR for EVA/CFR blends were reduced to 32%. According to this study, the design of fine structure might pave the way for the future development of halogen-free flame retardants combining both enhanced mechanical properties and excellent flame retardant behaviors.

KEYWORDS: *brucite, zinc borate, hierarchical structure, interfacial interaction, mechanical properties, flame retardant*

INTRODUCTION

In recent years, halogen-free flame retardants (HFFR) are commonly used to prepare flame-retarding polymers due to the healthy and environmental concerns.[1−6] Application examples of these flame-retarding polymer composites can be found in many industries including automotive, medical, electronic, building, and packaging.[7−14] Thus, developing various HFFR with multiple adaptability and high flame retarding efficiency is an important topic in these fields.

In the research for applied HFFR, mineral fillers, such as brucite and zinc borate, have attracted considerable attentions.[15−20] Natural brucite (mineral form of magnesium hydroxide) is an excellent non-toxic and smoke-suppressing HFFR with high decomposition temperature, which allows higher processing temperature in flame retardant (FR) polymer composites. Nevertheless, its fatal disadvantages are low flame retardant efficiency and high loading level (up to more than 60 wt %), which are detrimental to the mechanical properties,[21,22] especially strength in polymer composites containing brucite filler. Consequently, to obtain better comprehensive properties, great efforts have been made on brucite incorporated with other synergistic agents[23−34] to improve the mechanical properties[35] and flame resistance of polymer composites. One potential strategy is to mix brucite and zinc borates as HFFR.[23,24,30,33,34]

Received: January 18, 2014
Accepted: May 9, 2014
Published: May 9, 2014

 © 2014 American Chemical Society

Zinc borates have been reported as potential fillers to retard the thermal degradation of polymers because of their high thermal stability.[36−40] Previous studies demonstrated that there are major advantages and synergistic effects in using a combination of zinc borates with brucite in polymers.[30,33,34] As a result, zinc borates form a glassy cage for polymer chains as a physical barrier, which is benefit to the flame retardancy. However, these synergistic effects are based on simple physical mixing of zinc borates and brucite. It still needs a high loading amount of FR in polymers to fulfill the flame retardant specifications.[33] Meanwhile, the mechanical properties of polymer composites decrease sharply owing to the poor compatibility between FR particles and polymer matrix. To the best of our knowledge, no work has been reported on controllable fabrication of zinc borate [$Zn_6O(OH)(BO_3)_3$] hierarchical nanostructure on brucite particles' surface, fabricating brucite@$Zn_6O(OH)(BO_3)_3$ composite flame retardant (CFR) particles to significantly enhance the mechanical properties and flame retardant efficiency at the lower loading amount.

In our previous works,[41] we found that the core/shell structured brucite@polyphosphate@amine hybrid system could remarkably enhance the flame retarding efficiency even at the lower loading amount. However, the mechanical properties (especially tensile strength) were still far away from our expectation. Considering the lower water content and higher thermal stability (>600 °C) of $Zn_6O(OH)(BO_3)_3$, which was successfully prepared in large scale by our group,[42] in this paper, we attempted to synthesized $Zn_6O(OH)(BO_3)_3$ hierarchical nanostructure on brucite particles' surface through a simple and facile method, resulting in the formation of an obvious core (brucite)/shell [$Zn_6O(OH)(BO_3)_3$] nanostructure for great improvement of both the mechanical properties and flame retarding efficiency in polymers. The $Zn_6O(OH)(BO_3)_3$ hierarchical nanostructure, which looked like little anchor flukes, could implant into the polymer matrix (here we chose EVA) and played multiple roles by acting as not only a synergistic agent but also a structural reinforcer. In comparison with the simple physical mixture (PM) in the EVA matrices, the novel structure of CFR particles presented remarkable performance including both the mechanical properties and flame retardancy in EVA composites. The mechanisms for the improvement of mechanical properties and flame retardancy were also investigated in detail. To help all the FR particles disperse well in the EVA matrix, the γ-aminopropyltriethoxysilane (AMEO) was used (as a surface modified agent of the FR fillers). The first part of this paper concerned the evaluation of the CFR particles. In the second part, the mechanical properties and flame retardant behaviors were measured to elucidate these improvements resulting from the novel hierarchical nanostructure of the CFR particles.

EXPERIMENTAL SECTION

Materials. The brucite powder (2500 mesh) was kindly supplied by Sino Minmetals (China). It contains more than 95 wt % of magnesium hydroxide and the chemical components are listed in Table 1. The zinc vitriol ($ZnSO_4·7H_2O$, analytical grade) and borax ($Na_2B_4O_7·10H_2O$, analytical grade) were purchased from Tianjin Bodi Chemical Co., Ltd. (China). The sodium hydroxide (NaOH, analytical grade) flakes were purchased from Tianjin Beilian Fine Chemicals Development Co., Ltd. (China). The ethylene-vinyl acetate copolymer (TAISOX 7350M, 18 wt % of vinyl acetate) was supplied as pellets by Formosa Plastics Corporation and its melt index is 2.5 dg/min at 190 °C and 2.16 kg load. All of these materials were used as received without any further purification.

Table 1. Chemical Components of Brucite Powder

$Mg(OH)_2$ (wt %)	SiO_2 (wt %)	CaO (wt %)	Fe_2O_3 (wt %)	insoluble residues (wt %)
≥95	<2	<2	<0.5	<1.5

Preparation of Brucite@$Zn_6O(OH)(BO_3)_3$ Composite Flame Retardant Particles. The brucite@$Zn_6O(OH)(BO_3)_3$ composite flame retardant (CFR) particles were obtained by a facile and progressive growth method which was illustrated in Scheme 1. The possible reactions took place as follows:

$$Na_2B_4O_7 + 7H_2O \rightarrow 2NaOH + 4H_3BO_3$$

$$ZnSO_4 + 2OH^- \rightarrow Zn(OH)_2 + SO_4^{2-}$$

$$Zn(OH)_2 + 2OH^- \rightarrow Zn(OH)_4^{2-}$$

$$6Zn(OH)_4^{2-} + 3H_3BO_3 \rightarrow 12OH^- + Zn_6O(OH)(BO_3)_3 + 10H_2O$$

In a typical synthesis, 69.6 g (1.2 mol) of brucite powder was suspended in 200 mL deionized water and the slurry was heated in a water bath heating at 90 °C for 1 h. Then 200 mL of a 0.25 mol/L borax aqueous solution (excess) was added into the mixture slurry. After 10 min, 400 mL of a 0.25 mol/L zinc sulfate aqueous solution was injected into the slurry rapidly and a small amount of sodium hydroxide aqueous solution (4 mol/L) was added to the reaction system in drops to maintain the pH value of 7.5−8.0 for more than 6 h. Vigorous stirring was applied during the whole procedure. Finally, the suspension was immediately filtered and washed with deionized water (90 °C) several times to remove the water-soluble impurities until no SO_4^{2-} was detected by 1 mol/L $BaCl_2$ aqueous solution. The obtained products were dried under vacuum at room temperature for 24 h, yielding a loosened white powder.

Preparation of the $Zn_6O(OH)(BO_3)_3$. The $Zn_6O(OH)(BO_3)_3$ powder was obtained according to our previous works.[42] In a typical synthesis, 3.8 g (0.01 mol) of borax was dissolved in 30 mL deionized water in a water bath heating at 90 °C. Then 30 mL of a 0.33 mol/L zinc sulfate aqueous solution was injected into the borax aqueous solution rapidly and a small amount of sodium hydroxide aqueous solution (4 mol/L) was added to the reaction system in drops to maintain the pH value of 7.5−8.0 under continuous stirring for 6 h. Finally, the suspension was immediately filtered and washed with hot deionized water (90 °C) several times to remove the water-soluble impurities until no SO_4^{2-} was detected by 1 mol/L $BaCl_2$ aqueous solution. The obtained whitish product was dried under vacuum at room temperature for 24 h, yielding a loose $Zn_6O(OH)(BO_3)_3$ powder.

Preparation of the Physical Mixture. For comparison, the physical mixture (PM) was prepared by mixing brucite and $Zn_6O(OH)(BO_3)_3$ powder (Supporting Information Figure S1) with a high-speed mixer at room temperature. The weight content of $Zn_6O(OH)(BO_3)_3$ in the mixture was 12.3% (measured by ICP elemental analysis), similar to that in the CFR.

Preparation of EVA/Flame Retardant Composites. To well disperse all the flame retardant (FR) particles into the EVA matrices, surface modification was carried out. Flame retardant particles (30% weight ratio to ethanol) were added into grade ethanol (containing 4 wt % of water). Subsequently, the mixture was heated in a water bath for 1 h. Then the γ-aminopropyltriethoxysilane (AMEO) (3% weight ratio to FR) was feed into the reaction system, with vigorously stirring and refluxing for 2 h. The product was collected and washed with ethanol several times and then dried in a vacuum system at 50 °C for 12 h for subsequent blending.

The EVA/FR composites were prepared by melt mixing for 15 min at a temperature of 165 °C using an open mill as 200 g batches. The open mill has two exposed rotors running in a contra-rotating way to

Scheme 1. Schematic Illustration of Synthesis of Brucite@$Zn_6O(OH)(BO_3)_3$ Composite Flame Retardant (CFR) Particles

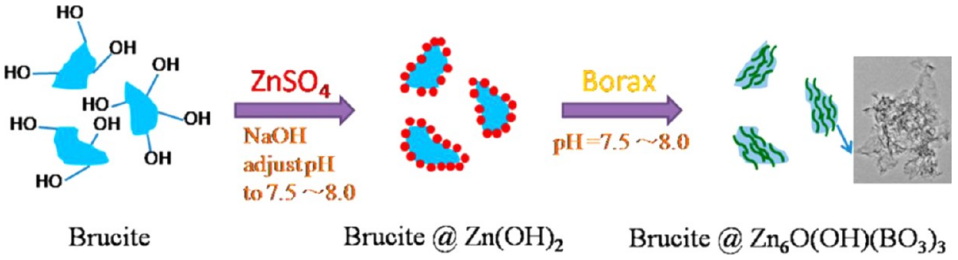

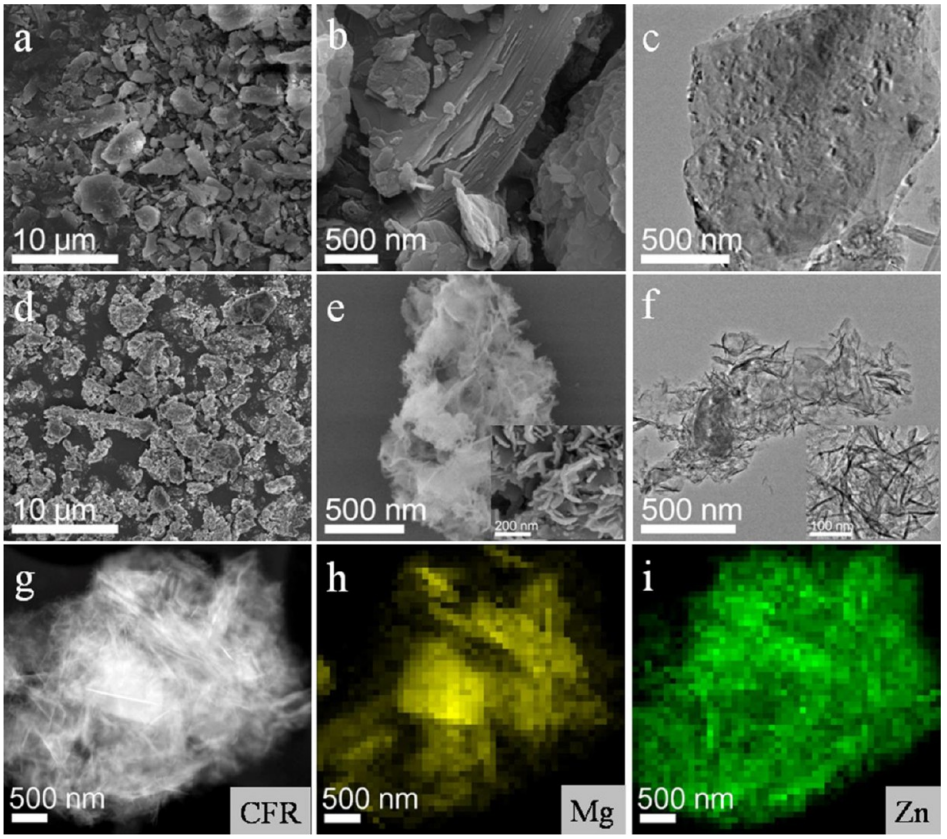

Figure 1. FESEM images of the (a) low and (b) high magnification views of the brucite particles. (d) Low and (e) high magnification views of the brucite@$Zn_6O(OH)(BO_3)_3$composite flame retardant (CFR) particles. TEM images of the (c) brucite particle and (f) CFR particle. TEM image of (g) a selected area of CFR particles and the corresponding elemental mapping analysis of (h) Mg and (i) Zn. The $Zn_6O(OH)(BO_3)_3$ hierarchical nanostructure, which located on the surface of brucite particle, could be clearly observed.

blend the surface-modified FR powders and EVA. Thereafter, sheets with 4, 3, and 1 mm thickness were obtained by compression molding under a pressure of 10 MPa at 155 °C for 30 min, respectively. The content of FR additives was varied from 0 to 60 wt %.

Characterization of the Powder Samples and EVA/FR Composites. The morphology of particles was carefully examined under field emission scanning electron microscopy (FESEM, Nova NanoSEM 450) and high-resolution transmission electron microscopy (HRTEM, Tecnai G2 F30) equipped with a FP 5360/30 HAADF Detector. The distribution of each element in the product was examined by high-angle annular dark-field scanning transmission electron microscope energy dispersive X-ray spectroscopy (HAADF-STEM-EDX) measurements at 300 kV. For the powders, nitrogen adsorption measurements were performed at 77 K, using a Micromeritics ASAP 2010 system utilizing Barrett−Emmett−Teller (BET) calculations for surface area. Powder X-ray diffraction (XRD) patterns of the particles were recorded on a Rigaku D/max 2400 system using Cu Kα radiation at 2θ values ranging from 5° to 80°. Thermal analysis was performed on a Mettler-Toledo TGA/SDTA 851e thermal analyzer at a heating rate of 10 °C/min from room temperature to 800 °C under a static air atmosphere. Fourier transform infrared (FTIR) spectra were recorded on a JASCO FT/IR-460 plus spectrometer using KBr disc method.

The freeze-fractured cross sections of EVA/FR composites, which were used to observe the interfacial interaction, were obtained by liquid nitrogen (−196 °C) quenching. And part of them was etched with hydrochloric acid for 2 h to remove the exposed inorganic particles. All the cryogenic fractured cross sections were coated with gold using vacuum sputter coater to improve the surface conductivity and then the images were obtained by FESEM.

Tensile tests were conducted on a JSL-5000N testing machine (Jiangdu Jingyi Test Instruments Co., Ltd., Jiangsu Province, China) at an extension rate of 200 mm/min at room temperature following the GB/T 1040-92 standard. The tensile strength (refers to the peak stress) and elongation at break were recorded. Before testing, the specimens were conditioned at room temperature at least 24 h. The test results were the average values of at least ten die-cut dumbbell specimens (1 mm thickness).

A TA Instruments AR-2000 Rheometer, in conjunction with an environmental testing chamber for temperature control and torsion

dx.doi.org/10.1021/am500380n | ACS Appl. Mater. Interfaces 2014, 6, 7223−7235

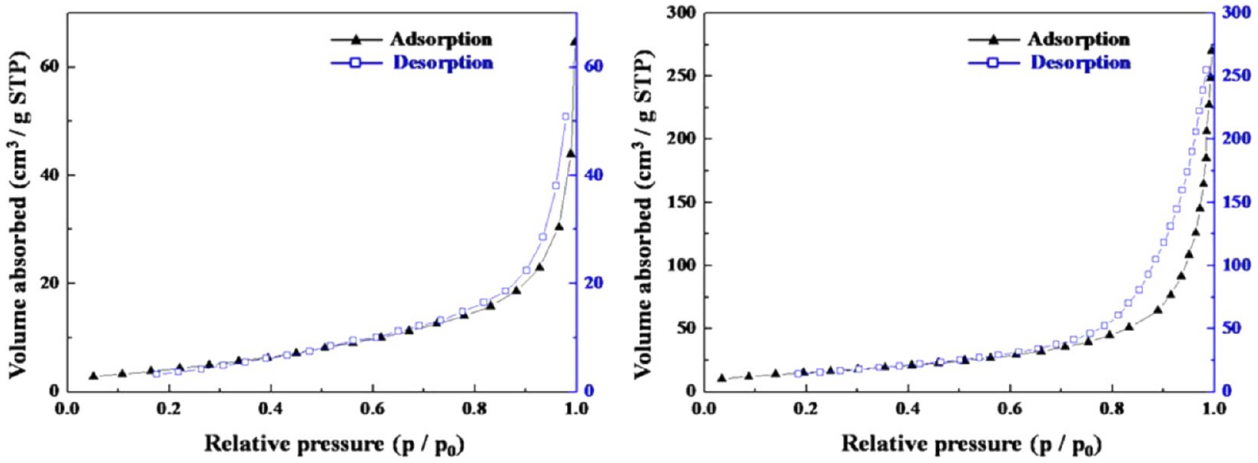

Figure 2. N_2-sorption isotherms for the brucite (left) and CFR (right) particles.

fixtures, was used to monitor the rheological response of specimens (50 × 13 × 2 mm^3). The measurements were conducted in an air atmosphere over the temperature range of 130−230 °C at a heating rate of 3 °C/min.

Flammability Tests of EVA/FR Composites. The UL-94 classification was carried out using a M607B type instrument (Qingdao Shanfang Instrument Co., Ltd., Shandong Province, China) on the specimens of 127 × 12.7 × 3 mm^3 according to GB/T 2408-2008.

The limiting oxygen index (LOI, Standard Test Method for measuring the minimum oxygen concentration to support candle-like downward flame combustion) measurements were carried out using an OJN-9307 type instrument (Shenzhen Test Machine Co., Ltd., Guangdong Province, China) on the specimens of 120 × 6.5 × 3 mm^3 according to GB/T 2406-2008. To estimate the error and to check the repeatability, the LOI values were measured 10 times for each sample.

The cone calorimeter from Fire Testing Technology (FTT, UK) was used to characterize the forced flaming behavior of EVA/FR composites under 35 kW/m^2 external radiant heat flux conforming to ISO 5660 standard. A 100 × 100 × 4 mm^3 sheet was exposed to a radiant cone (CONE).[43,44] The cone calorimeter brings quantitative analysis to materials flammability research. The flammability parameters considered in this study were: heat release rate (HRR), peak of heat release rate (PHRR), total heat released (THR), smoke production rate (SPR), mass loss rate (MLR), and char residue. Results corresponded to mean values obtained from 3 experiments for each formulation and were reproducible with variation less than 10%.

RESULTS AND DISCUSSION

Chemical Compositions and Structure Characterization. The morphologies and structures of the brucite and brucite@$Zn_6O(OH)(BO_3)_3$ composite flame retardant (CFR) particles were examined by FESEM and TEM. Typical images are shown in Figure 1. In the low magnification views (Figure 1a and 1d), numerous particles with micronmeter and nanometre sized diameter were stacked. The high magnified images (Figure 1b and 1e) displayed the different surface morphologies between brucite and CFR particles. Figure 1b and 1c showed that the brucite particles were angular and irregular in shape owing to the physical comminution of brucite ore. In contrast, it was observed that CFR particle (Figure 1e and 1f) had an obvious hierarchical nanostructure consisting of interconnected and primary nanoflakes on the particle surface. Moreover, the inset clearly revealed that the hierarchical structure, like many little anchor flukes, was built up by nanoflakes with the size of about 100 nm and thickness of 10−20 nm. This meant that these anchor flukes could easily embed into the polymer matrix and provide polydirectional internal stress transfer. On the other hand, this hierarchical surface nanostructure might bring higher surface area. Thus, the control samples were examined by N_2 sorption measurement. Representative nitrogen desorption/adsorption isotherms of brucite and CFR particles are shown in Figure 2. The brucite particles had a low BET specific surface area of 15 m^2/g, while the CFR particles revealed a high BET specific surface area of 65 m^2/g.

The powder XRD patterns of brucite, CFR, and $Zn_6O(OH)(BO_3)_3$ (Figure 3) were measured to identify the

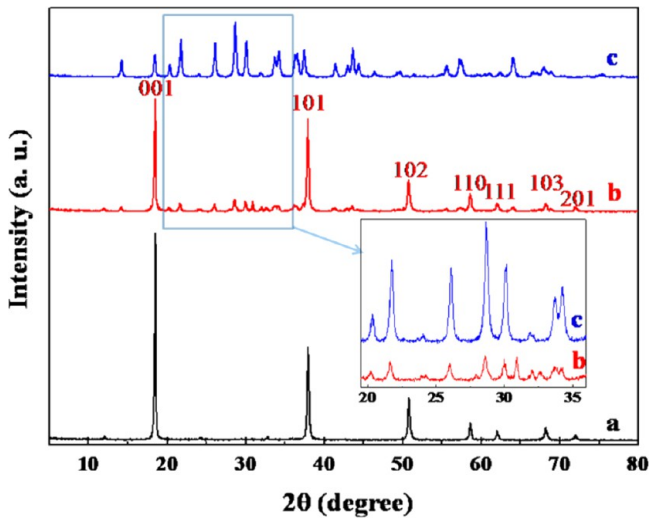

Figure 3. XRD parttens of (a) brucite, (b) CFR, and (c) $Zn_6O(OH)(BO_3)_3$.

hierarchical nanostructure locating on the surface of CFR particles. It could be seen that the CFR particles presented characteristic reflections of both the brucite and $Zn_6O(OH)(BO_3)_3$ phases. The main characteristic peaks of CFR correspond to the diffractions by (001), (101), (102), (110), (111), (103), and (201) planes indexed to the typical hexagonal structure of raw brucite with the lattice constants comparable to the values of JCPDS 44-1482. It was noted that the intensities of the characteristic reflections for CFR were obviously weakened compared to those in brucite phase, resulting from a plausible coverage for the surface hierarchical nanostructure

to some extent. Meanwhile, the diffraction peaks of CFR could match well with the pure $Zn_6O(OH)(BO_3)_3$,[45,46] indicating that the in situ synthesized hierarchical nanostructure indexed to the $Zn_6O(OH)(BO_3)_3$ phase and encapsulated the brucite surface (Scheme 1 and Figure 1). And the EDX elemental mapping images (Figure 1g–i) gave the direct evidence to above deduction.

The TGA and FTIR analyses are shown in Figures 4 and 5, respectively. As revealed in Figure 4, the thermal decomposition of physical mixture (PM) or CFR mainly took place in two weight loss steps. The first decomposition step (347–445 °C) of CFR corresponding to the decomposition of $Mg(OH)_2$ to MgO occurred at higher temperature than the PM (340–436 °C). Meanwhile, the derivative weight peak of CFR was observed near 403 °C, which was 7 °C higher than that of brucite and PM. In other word, during the first step of decomposition, CFR particles present a higher thermal stability.

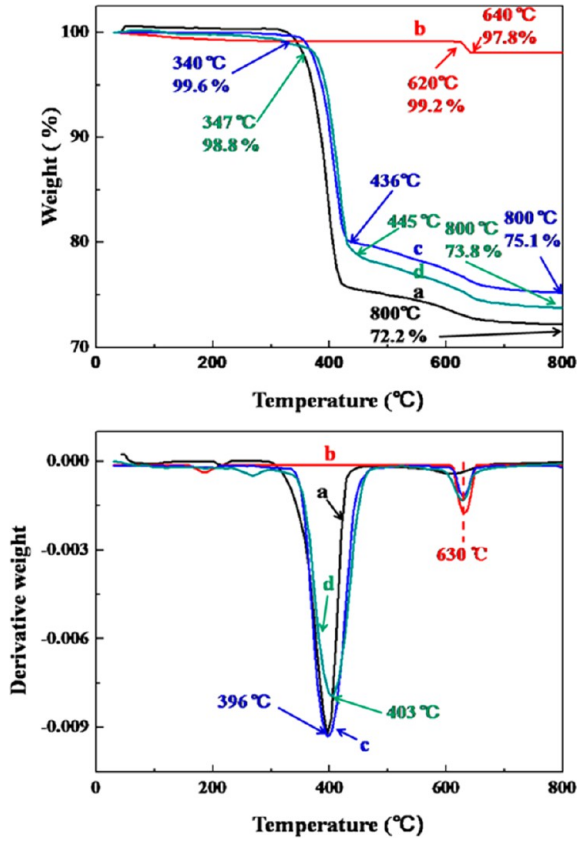

Figure 4. TGA/DTG curves of (a) brucite, (b) $Zn_6O(OH)(BO_3)_3$, (c) PM, and (d) CFR.

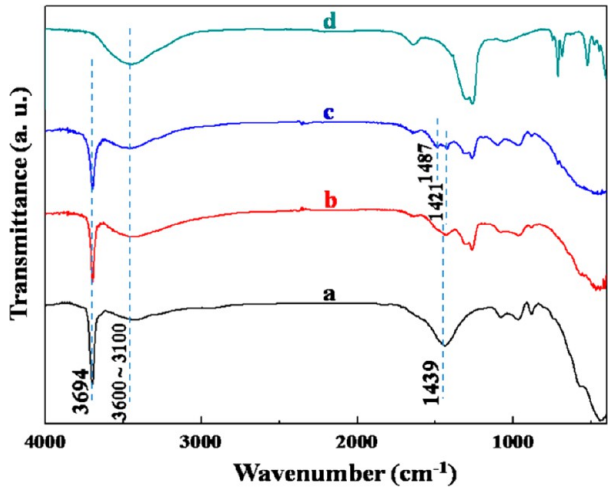

Figure 5. FTIR spectra of (a) pristine brucite, (b) PM, (c) CFR, and (d) $Zn_6O(OH)(BO_3)_3$.

The FTIR spectra gave the evidence to this assumption shown in Figure 5. The brucite and CFR showed strong absorbances at 3694 cm^{-1} owing to the stretching vibration bands for free hydroxyl groups, while the synthesized $Zn_6O(OH)(BO_3)_3$ only presented a wide absorption at 3600–3100 cm^{-1} corresponding to the stretching vibration bands for associating hydroxyl group. In comparison of PM, it was worth noting that this absorbtion of CFR were slightly decreased in intensity. Additionally, the characteristic absorption of 1439 cm^{-1} (Figure 5a) was assigned to the stretching vibration band of C–O—Mg resulting from the chemisorbed CO_2 on the surface of raw brucite. However, this absorption split and shifted to wavenumbers of 1487 and 1421 cm^{-1} (Figure 5c) because of the formation of Zn–O—Mg and B–O—Mg modes through the dehydration[41] between surface hydroxyl group of material brucite and synthesized $Zn_6O(OH)(BO_3)_3$ hierarchical nanostructure. It confirmed the conclusion based on the TGA analysis that the chemisorbed coverage resulted in a higher thermal stability of CFR particles.

Moreover, the following stage of weight loss from 620–640 °C (Figure 4) was attributed to the decomposition of $Zn_6O(OH)(BO_3)_3$ and a corresponding derivative weight peak was observed around 630 °C. As for CFR, the final loss weight was slightly distinct from that of PM related to the content of bound water. This implied that the CFR particles showed more intense adsorbability for water because of the hierarchical nanostructure. On the basis of these analyses, we could conclude that the CFR particles was not a simple mixture of brucite with $Zn_6O(OH)(BO_3)_3$, but a new hybrid composite probably with excellent interface strength in polymer matrix.

Mechanical Properties and Interfacial Interaction. To evaluate the reinforcing effect of CFR particles on the EVA matrix, mechanical properties during extension were measured. The introduced γ-aminopropyltriethoxysilane (AMEO), which played a role as a coupling agent, was used to prevent aggregation of FR particles in EVA matrix and improve compatibility between FR particles and EVA. Indeed, the surface treatment of FR particles by AMEO could reduce the surface free energy to some extent,[47] resulting in an increase in the degree of dispersion of the FR particles. Concurrently, it could ensure the same dispersion degree of all the FR particles in EVA matrix and prevent from unparallel deterioration of mechanical properties caused by the different dispersion degree. Because of the unique surface structure of multidentate hierarchical nanostructure and the very high surface area in the EVA/CFR composites, the applied stress is expected to be easily transferred from the EVA matrix onto the CFR particles, resulting in a remarkable enhancement of the mechanical properties.

The mechanical properties of EVA blended with the four kinds of FR are shown in Figure 6. As to the EVA elastomer, the tensile strength (TS) and elongation at break (EAB) were always taken into account. Generally, the mechanical properties of EVA/FR composites decreased considerably with the addition of FR particles. This could be attributed to the poor

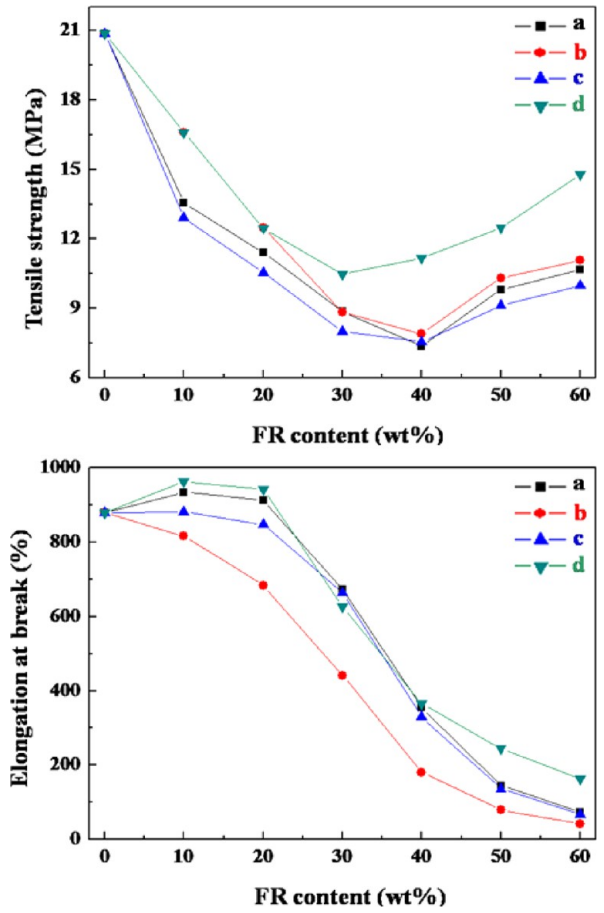

Figure 6. Mechanical properties of sample (a) EVA/brucite, (b) EVA/$Zn_6O(OH)(BO_3)_3$, (c) EVA/PM, and (d) EVA/CFR formulations.

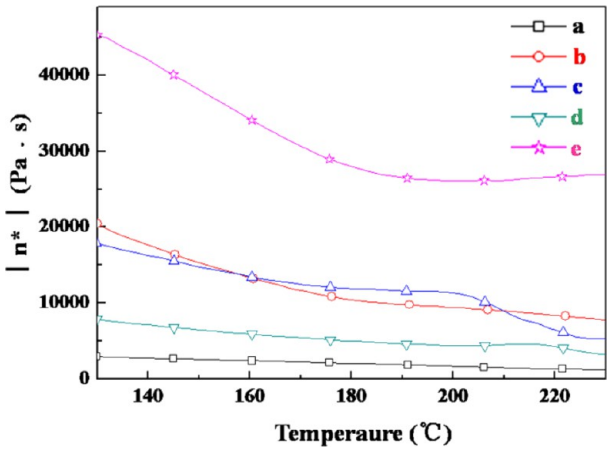

Figure 7. Viscosity curves for (a) pure EVA, (b) EVA/brucite, (c) EVA/$Zn_6O(OH)(BO_3)_3$, (d) EVA/PM, and (e) EVA/CFR formulations. The loading amounts of FR particles were all kept constant at 45 wt %.

compatibility of the added FR particles with the polymer matrix even in the presence of a coupling agent. That was why the TS rapidly decreased with the increasing FR content from 10 to 30 wt %. Conversely, with the addition of FR particles from 40 to 60 wt %, gradual increases in TS were observed probably resulting from a competition between the interfacial interaction (or friction effect) and the poor compatibility. Concurrently, it made the EVA composites become stiffer. Interestingly, it was worth noting that the EVA/CFR formulation exhibited a minimum in TS at the concentration of 30 wt %, while the EVA/brucite, EVA/$Zn_6O(OH)(BO_3)_3$, and EVA/PM formulations showed this minimum with the contents up to 40 wt %. This phenomenon might cause by the unique surface hierarchical nanostructure, which could implant into the EVA matrix and allow an increasing contact area. Both permitted a much more efficient transfer of stress from the EVA matrix to the FR particles. As to EVA/CFR composite, TS and EAB were more sensitive to the nanostructure of the EVA composites. Comparing the EVA/FR composites, a dramatic increase in TS was observed for EVA/CFR formulation with any loading amount, reaching at least a 20% increment in comparison with EVA/brucite, EVA/$Zn_6O(OH)(BO_3)_3$, and EVA/PM formulations. It gave the best evidence for the reinforcing function of surface hierarchical nanostructure. More importantly, this reinforcing function was also reflected in the molten state. The rheological measurements presented a comparatively high viscosity of EVA/CFR blends (Figure 7), which brought some advantages in droplet inhibition and char forming. Additionally, the EVA/CFR formulation showed a positive impact on the EAB, especially at the higher FR loading (40−60 wt %). It might be attributed to the multiple orientations of hierarchical surface nanostructure, which could prevent the micro cracks from propagating at the interface. Namely, it revealed that the nanoscale of inorganic fillers could improve the compatibility between filler particles and polymer matrix. The later FESEM images of composite cross sections gave more details about these improvements.

Filler adhesion with the polymer matrix, either in physical or chemical interaction, is of great importance for improving the mechanical properties of polymer composites. Fine control of the interfacial contact of polymer composites is one of the most critical strategies to impart desired mechanical properties to such materials.[48−50] To explain the behaviors of the EVA/FR composites, the cross sections of the three EVA/FR blends were examined with FESEM shown in Figure 8, when the loading of FR particles was kept constant at 60 wt %. The images of the fractured surface of EVA/brucite, EVA/PM, and EVA/CFR composites (Figures 8a−c) showed relatively smooth surface which was distinct from the untreated one (Supporting Information Figure S2). With the low concentration of AMEO on the surface of the FR particles, the dispersion was significantly improved and no obvious aggregates or cavities were observed which was in agreement with previous literatures.[51] After etching by hydrochloric acid, a lot of apparent cavities were observed in the cross sections of EVA/brucite (Figure 8d) and EVA/PM (Figure 8e) composites. It revealed that, the filler particles showed poor interface adhesion with EVA matrix, which acted as stress concentrators of failure points of the composites. More frequently, the fracture occurred along the phase boundary between EVA matrix and FR particles resulting in exposing of the FR particles and less transfer of stress from the EVA matrix to the FR particles. This could be related to the inferior mechanical properties. However, in the case of EVA/CFR composite (Figure 8f), few etched holes were detected even at the highest content of 60 wt %. Indeed, the CFR particles seemed to be embedded into the EVA matrix and showed well interface adhesion with EVA matrix. As explained before, the presence of the hierarchical surface nanostructure could significantly improve the interfacial interaction and the transfer

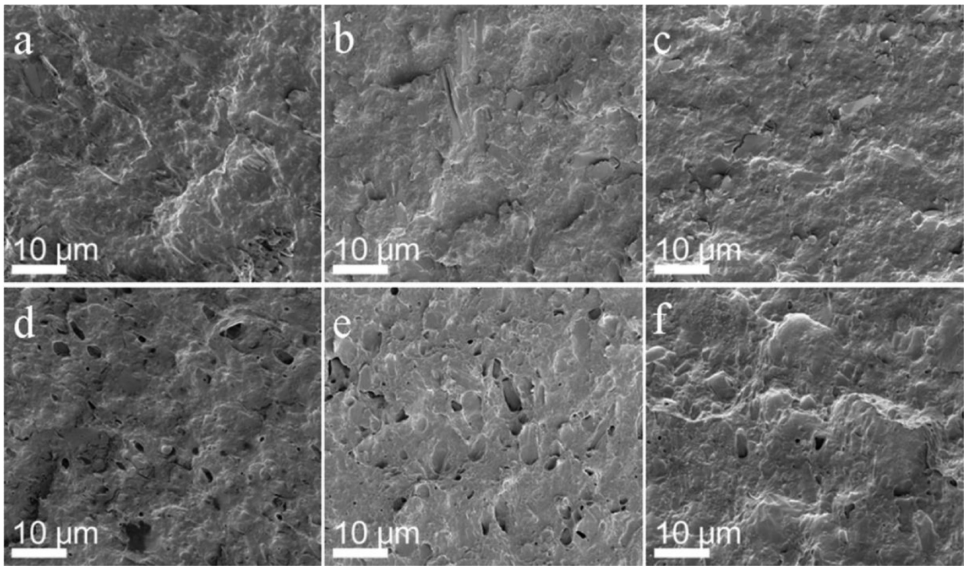

Figure 8. FESEM images of freeze-fractured cross sections. (a) EVA/brucite and (d) EVA/brucite etched by hydrochloric acid; (b) EVA/PM and (e) EVA/PM etched by hydrochloric acid; and (c) EVA/CFR and (f) EVA/CFR etched by hydrochloric acid. The loading amounts of FR particles were all kept constant at 60 wt %.

of stress between CFR particles and EVA matrix. It could thus be proposed that the stress was well dispersed in the EVA composite and the fracture occurred from the unsubstantial parts of the EVA matrix. Consequently, the mechanical properties were markedly improved in comparison with that of EVA/brucite and EVA/PM formulations.

Flammability of the EVA/FR Composites. The unique hierarchical surface nanostructure of brucite@$Zn_6O(OH)(BO_3)_3$ composite flame retardant (CFR) not only improved mechanical properties but also highly increased the flame retardant of EVA composites. The limiting oxygen index (LOI) and vertical burning test (UL-94) data on different loading of flame retardant (FR) particles in five kinds of formulations are given in Table 2. It could be observed that the LOI values of EVA/FR composites were improved with the increasing loading amount of any FR particles. At the equivalent FR contents, the EVA/CFR formulation displayed the highest LOI values, which might be ascribed to highest viscosity of the EVA composite caused by the unique surface structure of CFR particles (Figure 7). In contrast, it was clear that the LOI values of EVA/PM formulations were parallelly lower than those of EVA/brucite formulations, which was in accordance with the previous study.[24] Additionally, as for both EVA/brucite and EVA/PM composites, no UL-94 V rating could be achieved mainly due to the presence of melt dripping (mainly caused by low viscosity) (Supporting Information Figure S3a and S3b). Conversely, the EVA/CFR composite was seen to resist ignition and subsequent combustion (Supporting Information Figure S3c), which could reach UL-94 V rating in all cases showing an excellent synergy. These remarkable performances indicated that the best flame retardancy was obtained for EVA/CFR formulation in which the $Zn_6O(OH)(BO_3)_3$ hierarchical surface nanostructure existed, facilitating an increase of the viscosity of EVA composites. It was worth noting that the LOI value of EVA/CFR composite filled with 45 wt % was still up to 33, while the corresponding formulations with EVA/brucite, EVA/$Zn_6O(OH)(BO_3)_3$, and EVA/PM were only 25, 21, and 24, respectively. Apart from that, only the EVA/CFR composite could pass the V-0 rating of the UL-94 test with this low loading amount. In other word, the EVA/CFR composite with addition of 45 wt % could be regarded as the fire retarding material, which met the industrial standard of cable material.

Table 2. LOI and UL-94 Data of EVA/Brucite, EVA/$Zn_6O(OH)(BO_3)_3$, EVA/PM, and EVA/CFR Formulations

	composition (wt %)			
sample formulation	EVA	FR	LOI	UL-94
virgin EVA	100	0	17	fail
EVA/brucite	60	40	23	fail
	55	45	25	fail
	50	50	27.5	fail
EVA/$Zn_6O(OH)(BO_3)_3$	60	40	19	fail
	55	45	21	fail
	50	50	24	fail
EVA/PM	60	40	22	fail
	55	45	24	fail
	50	50	27	fail
EVA/CFR	60	40	29	V-2
	55	45	33	V-0
	50	50	35.5	V-0

To elucidate the intrinsic reasons for the enhancement of flame resistance by the unique structure of CFR particles, cone calorimeter test was examined.[52] The cone calorimeter test is one of the most effective bench-scale methods to study the flammability of polymer composites. With the equivalent FR content of 45 wt %, four control samples including EVA/brucite (A1), EVA/$Zn_6O(OH)(BO_3)_3$ (A2), EVA/PM (A3), and EVA/CFR (A4) formulations along with pure EVA (A0), were repeated three times and the deviation of their data was within ±10 %. Heat release rate (HRR), peak heat release rate (PHRR), total heat released (THR), smoke production rate (SPR), mass loss rate (MLR), and char residue were simultaneously obtained to evaluate the flame retardancy of EVA/FR composites.

Figure 9 presented the dynamic curves of HRR versus time for the samples of A0, A1, A2, A3, and A4. It could be found

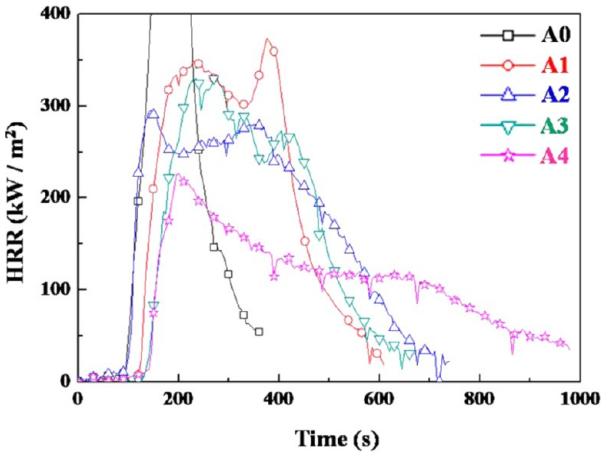

Figure 9. HRR curves for A0, A1, A2, A3, and A4.

that the sample A1 burned out within 610 s after ignition. Two obvious HRR peaks were observed at the range of 110−610 s with PHRR of 348 and 373 kW/m^2, respectively. Indeed, the second PHRR could be ascribed to a thin and fragile MgO layer with holes and cracks. During complete combustion, this crisp structure almost collapsed (Figure 13a) resulting in promotion of heat radiation and gaseous phase transfer. It could be proposed that the second PHRR came from explosive combustion resulting from the sufficient contact between oxygen rushing through the collapsed structure and combustible gases stored under the protective layer. As to sample A3, physical mixture of brucite and $Zn_6O(OH)(BO_3)_3$ powders showed a unconspicuous decrease in PHRR with various stages from 273 to 332 kW/m^2 and was no more effective than an individual brucite; it meant that there was no obvious synergistic interaction. These result further indicated an unstable and fragile protective layer (Figure 13b) which could not prevent heat transfer and gaseous diffusion effectively. Generally, to obtain a stable and insulating layer to significantly reduce the HRR with such physical mixture system, the total content of FR must reach 60 wt % including 40 wt % of brucite and 20 wt % of zinc borate.[30] However, with the 45 wt % content of CFR particles [exactly combining 39.5 wt % of brucite and 5.5 wt % of $Zn_6O(OH)(BO_3)_3$] in EVA matrix, a dramatic decline of HRR intensities were observed. More importantly, sample A4 presented only one obvious PHRR of 226 kW/m^2 which was 32 % lower than that of sample A3; this superior effect of the CFR on PHRR reduction could be attributed to a remarkably synergistic action between brucite and $Zn_6O(OH)(BO_3)_3$ that favored the formation of compact char layer (Figures 13c and 14g). In addition, the combustion time of A4 was prolonged to 980 s from the 665 s of A3. After extinction of the flame (> 865 s), a smaller but still positive HRR value was observed, which could be ascribed to an oxidation process of the carbon-rich residue (afterglow). Through the whole combustion process, the gentle decline of HRR in sample A4 suggested that burning of EVA composite was gradually barriered due mainly to the formation of thick and stable char layer.

To evaluate the effect of the high surface area by CFR itself, we have synthesized magnesium hydroxide nanoneedles (Supporting Information Figure S4) with high specific surface area for PM according to our previous work[53] for a fair comparison. The results (Supporting Information Figure S5) indicated that high surface area could only improve the LOI value (no significant effect on UL94 rating and HRR). In this regard, the synergistic effect between the $Zn_6O(OH)(BO_3)_3$ hierarchical surface nanostructure and the internal brucite gave the best flame retarding performance.

The dynamic curves of THR and MLR are shown in Figures 10 and 11, respectively. With the equivalent FR content, the

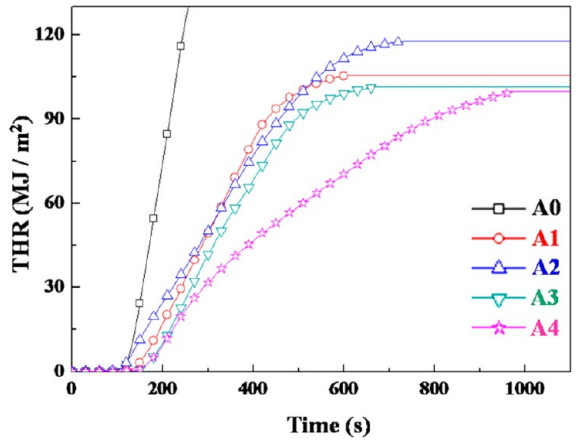

Figure 10. THR curves for A0, A1, A2, A3, and A4.

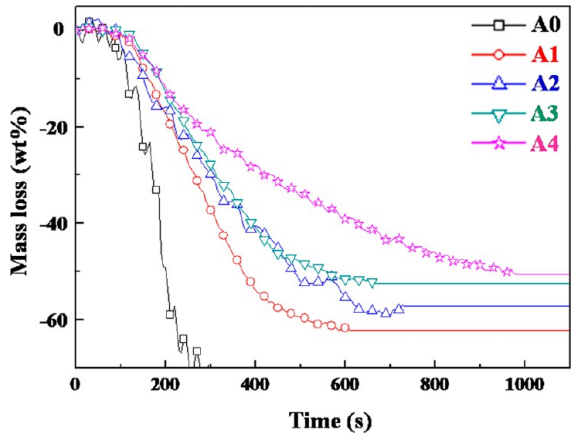

Figure 11. MLR curves for A0, A1, A2, A3, and A4.

THR of sample A4 was the lowest in the five control samples and the total burning time is also obviously prolonged. It meant that the heat of burning transfer was absorbed or barriered by the condensed phase effect of the additives.[54] Accordingly, the thermal degradation of EVA/CFR composites was effectively prohibited and the MLR analysis well confirmed this result which is shown in Figure 11. The addition of $Zn_6O(OH)(BO_3)_3$ (zinc borate) in EVA matrix had some benefits on the reduction of MLR and the increase of char residue. After complete combustion in cone calorimetry, the final mass loss of sample A1 was 62 wt %. In contrast, sample A3 and A4 was 53 and 50 wt %, respectively. The reason for these results was that the zinc borate could lead to a tenfold increase in rigidity and form a glassy foam structure[33,55] in fire. This glassy foam structure could accelerate charring of polymer chains. Generally, in order to obtain a stable glassy foam structure with physical mixture formulation, the total content of FR must reach 60 wt % including 40 wt % of brucite and 20 wt % of zinc borate.

To avoid the secondary hazards of smoke and meet the environmental requirements, the most significance of brucite

FR is the smoke suppression owing to the formation of active MgO layers in fire.[15,54,56] The dynamic curves of SPR for the five control samples are shown in Figure 12. Because of the low

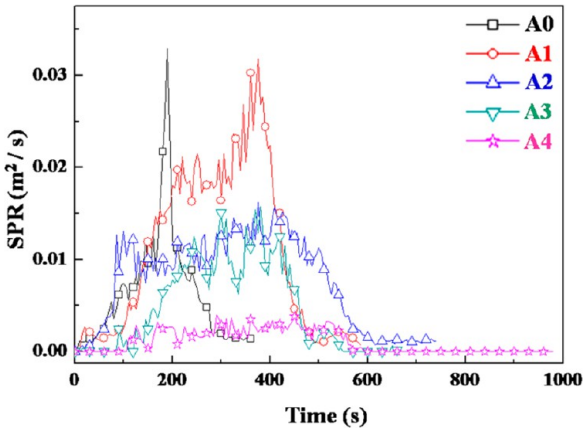

Figure 12. SPR curves for A0, A1, A2, A3, and A4.

BET specific surface area (Figure 2) and the collapse of char residue caused by the serious agglomeration of MgO particles (Figure 13a and b), the SPR of sample A0, A1, A2, and A3 was much higher than that of sample A4. It could be seen that the peak SPR value of sample A4 (0.004 m^2/s) was considerably reduced compared to that of sample A0 (0.033 m^2/s), A1 (0.032 m^2/s), A2 (0.016 m^2/s) and A3 (0.016 m^2/s), which implied that the shell $Zn_6O(OH)(BO_3)_3$ of CFR particles could prevent the active MgO particles from agglomerating in burning and bring more advantages of dispersity of MgO particles in the stable char residue. In this special case, the absorption of smoke could highly improve by the increasing specific surface area of active MgO. Apparently, the above results further demonstrated that this integrated structure of CFR particles could bring strong impact on flame retardancy and smoke suppression during polymer burning.

On the basis of the HRR analysis (Figure 9), it could be observed that the suppression of heart release was pronounced for the structure of CFR particles (A4) which exhibited significant longer burning time and only one apparent peak. It could be thought that the formed residue was seemingly large to demonstrate an insulating layer effect. The appearance of fire residues displayed by digital pictures in Figure 13 verified this suggestion. The combustion residual chars of sample A1 and A3 internally collapsed and displayed hollow structures (Figure 13a and b). The reason for this phenomenon might be that these formulations had low viscosity (Figure 7) and the melt of the blends was changed into deformable fluid more easily in fire. It was worth noting that the molten mass produced during the burning process was easy to migrate. Indeed, the active MgO particles generated from brucite decomposition also tended to migrate and aggregate containing in such molten mass (Figure 14a and e). Before forming an effective charring layer, the molten mass began to drip from the matrix taking out the char and the MgO particles. In other word, the chars were not enough cohesive to overcome the dripping of the polymer compositions, which was responsible for the fail in UL-94 test. These residual chars could also be described as thin and fragile layers that light mechanical stress (a finger touch was enough) caused these structures to crumble to dust. Both of them could not segregate oxygen and combustible gases effectively. And it

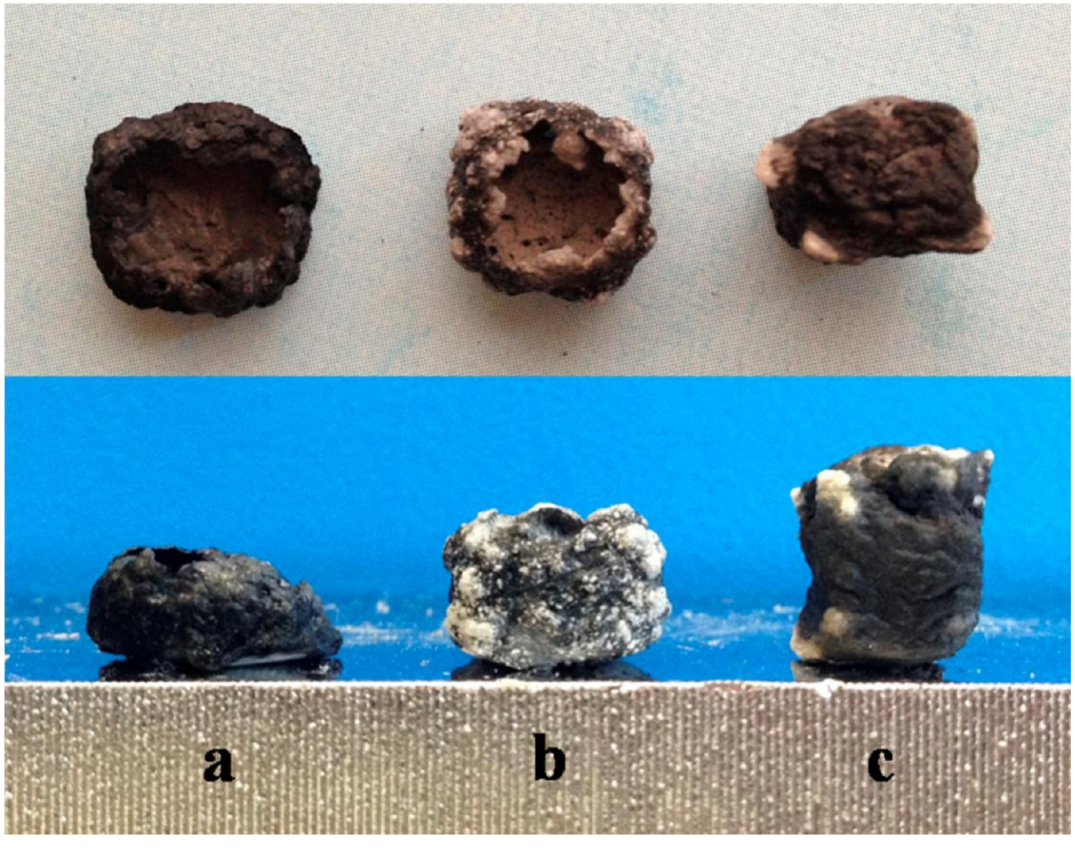

Figure 13. Digital pictures of combustion residues: (a) A1, (b) A3, and (c) A4.

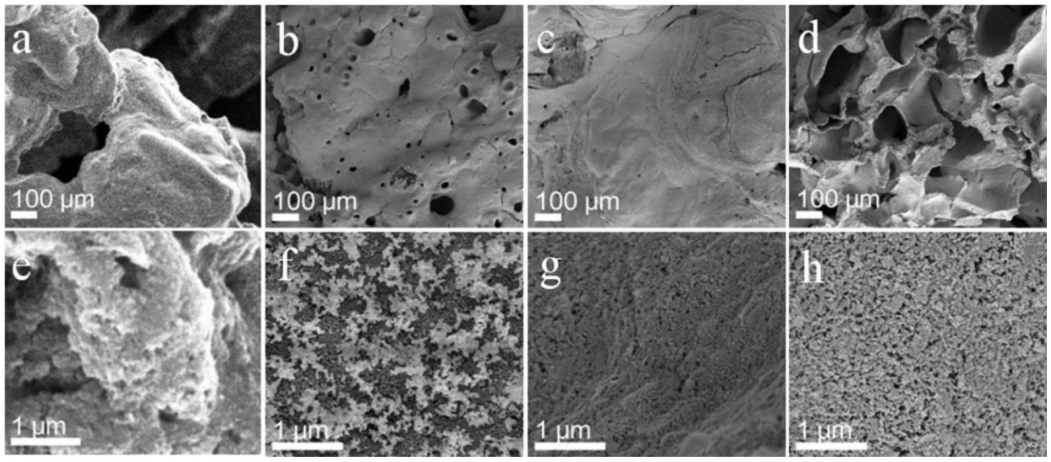

Figure 14. FESEM images of residual char obtained by cone calorimetry alternative. (a) Low and (e) high magnification views of sample A1. (b) Low and (f) high magnification views of sample A3. (c) Low and (g) high magnification views of sample A4. (d) Low and (h) high magnification cross sections of sample A4.

Scheme 2. Schematic Illustration of the Mechanism for the Enhanced Flame Resistance of the Brucite@$Zn_6O(OH)(BO_3)_3$ Composite

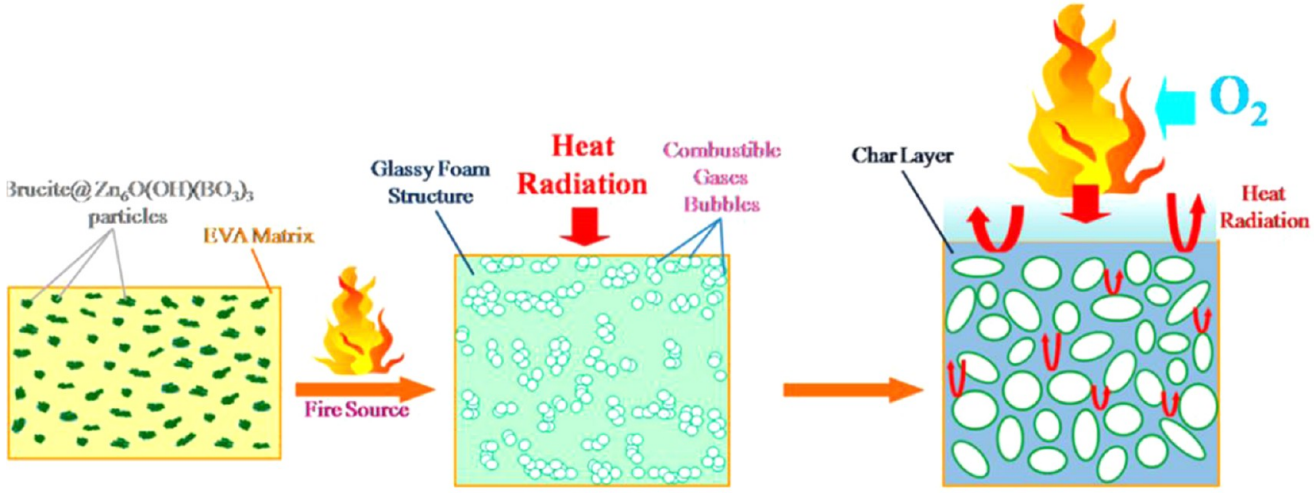

was also responsible for the second HRR peaks (Figure 9) because of oxygen diffusion through the collapsed layers. Conversely, the residue char of the sample A4 (Figure 13c) was homogeneous, compact and thick. The high intumescent ratio and rigidity (the residue can be handled without care) suggested that the flammable gases could hardly permeate through the char layer. This was the main reason for the significant decrease of HRR (Figure 9).

To explore the flame retardant mechanism of FR additives in EVA matrix, the char residues after complete combustion for the three FR systems were investigated by FESEM, as shown in Figure 14. The residue of sample A1 (Figure 14a and e) tended to aggregate together with lots of cracks and holes mainly because of the lack of tackifier or structural stabilizer (like zinc borate). This was in agreement with previous studies[54,57] which revealed MgO might sever as a discontinuous barrier. This kind of not enough stable and compact char layer was not effective to prevent the underlying EVA from degradation during combustion. As to the residue of sample A3, it could be seen that the residual char layer was continuous with some holes in the surface (Figure 14b) because the heated $Zn_6O(OH)(BO_3)_3$ (zinc borate) could form a glassy foam structure[33,55] and provide a stable softened glassy coating on the surface of the EVA under fire condition. Unfortunately, owing to the insufficient of $Zn_6O(OH)(BO_3)_3$ (only 5.5 wt %) in this physical mixture system, the $Zn_6O(OH)(BO_3)_3$ glassy foam was discontiguous on the surface of MgO layer (Figure 14f); thus the major structure of char residue also collapsed (Figure 13b). On the contrary, it was obvious that the residual char layer from sample A4 (Figure 14c and g) was more compact and continuous with a glassy film covering the surfaces which might be helpful for the quality of the char layer and maintain the main structure more stable with a remarkable expansion in volume (Figure 13c). This suggested that the internal released combustible gases could be prevented from passing through, resulting in an intumescent char (Figure 13c). The barrier effect of the stable char structure (Figure 14c and g) could also reduce the HRR and THR which was in accord with the heat release behavior. In addition, the interior morphologies of residue A4 were also important. In the low magnification view (Figure 14d), the presence of big cavities (about 100 μm) was observed in the interior residue, which was due largely to the bubbling of combustible gases in the degraded EVA matrix under fire condition. And the internal surface of a cavity (Figure

14h) was also compact and firm resulting from the extrusion of the bubble. In comparison with the residue A3 (Figure 13b), this internal microstructure might lead to a stable char layer and bring more benefit in thermal insulation.[58] Interestingly, this remarkable performance was only ascribed to the novel $Zn_6O(OH)(BO_3)_3$ hierarchical surface nanostructure of CFR particles. In general, the different residue's morphologies correlated quite well with the shape of HRR curves. The strong nature of the char formed from EVA/CFR formulation provided a condensed phase mechanism in flame retardancy as discussed above.

Flame Retardant Mechanism. The detailed mechanism on the enhanced flame resistance of the brucite@$Zn_6O(OH)(BO_3)_3$ composite nanostructure was proposed as Scheme 2. And the flame retardant mechanism in EVA composites in the presence of mineral fillers were believed to take place in the condensed phase because of the formation of a barrier layer from degraded EVA reinforced by mineral fillers. In the presence of CFR particles in EVA matrix, the $Zn_6O(OH)(BO_3)_3$ (zinc borate) hierarchical surface nanostructure could significantly improve the interfacial interaction and mechanical property of the EVA/CFR blends. The highly viscous melt of EVA should be formed in situ within the condensed phase in the initial stage of polymer composites burning. Concurrently, it could prevent the melt from changing into a deformable fluid at the high temperature. With the proceeding of combustion, a glassy foam structure was formed by the heated $Zn_6O(OH)(BO_3)_3$, resulting in an increase in rigidity of the condensed phase. Subsequently, the evolution of flammable gases which derived from degradation of EVA was blown into this highly viscous mixture and made many bubbles, the internal diffusion of which was able to make the bubbles bigger to form some cavities, further increasing the local concentration of the glassy foam. The net concentration of the glassy foam further increased along with the grown bubbles (Figure 14d). Surprisingly, the total 5.5 wt % content of $Zn_6O(OH)(BO_3)_3$ can lead to rapid charring of polymer chains. Obviously, such microstructure of the char layer could prevent contact between stored combustible gases and external oxygen. And the external heat radiation from burning area to the undegraded EVA was also barriered or slowed down. When a large amount of these char layer formed from the burning zone, the combustion would be difficult to maintain.

CONCLUSION

In summary, $Zn_6O(OH)(BO_3)_3$ hierarchical nanostructure was successfully synthesized on the surface of brucite particles, fabricating brucite (core)@$Zn_6O(OH)(BO_3)_3$ (shell) composite flame retardant (CFR) particles. In comparison with the simple physical mixture (PM), the unique hierarchical nanostructure could be easily implanted into the EVA matrix and highly enhance the interfacial interaction. This modification not only improved the mechanical properties but also increased the flame retardancy of the EVA/CFR composite even when the total loading of CFR was kept at the low value of 45 wt % (exactly including 39.5 wt % of brucite and 5.5 wt % of $Zn_6O(OH)(BO_3)_3$). On the basis of the massive evidence, the mechanism for the enhanced mechanical properties and flame resistance of CFR particles was proposed. All the results indicated this unique design might be developed as a new approach to green flame retardant materials.

ASSOCIATED CONTENT

Supporting Information

FESEM images of brucite and as-prepared $Zn_6O(OH)(BO_3)_3$ particles, FESEM image of freeze-fractured cross section of EVA/pristine brucite composite, the optical photographs after the UL-94 vertical burning test, TEM image of as-prepared magnesium hydroxide nanoneedles, and the LOI, UL94, and HRR analyses of EVA/PM (mixing magnesium hydroxide nanoneedles and $Zn_6O(OH)(BO_3)_3$) and EVA/CFR blends at the same content of 45 wt %. This material is available free of charge via the Internet at http://pubs.acs.org.

AUTHOR INFORMATION

Corresponding Author

*Tel./Fax: +8641184986067. E-mail: ninggl@dlut.edu.cn.

Notes

The authors declare no competing financial interest.

ACKNOWLEDGMENTS

G.L.N. and other authors thank Fundamental Research Funds for the Central Universities of China (DUT14RC(3)040 and DUT13RC(3)043), the NSFC (21276046), and the Ministry of Education Science and technology research projects and High-Tech R&D projects in Magnesium Industry of Liaoning Province (China) for financial support. Furthermore, the authors gratefully acknowledge senior engineer Xiaoxia Gao for TEM characterization, Dalian University of Technology.

REFERENCES

(1) Bitinis, N.; Hernandez, M.; Verdejo, R.; Kenny, J. M.; Lopez-Manchado, M. A. Recent Advances in Clay/Polymer Nanocomposites. *Adv. Mater.* **2011**, *23*, 5229−5236.

(2) Waaijers, S. L.; Bleyenberg, T. E.; Dits, A.; Schoorl, M.; Schütt, J.; Kools, S. A. E.; Voogt, P. D.; Admiraal, W.; Parsons, J. R.; Kraak, M. H. S. Daphnid Life Cycle Responses to New Generation Flame Retardants. *Environ. Sci. Technol.* **2013**, *47*, 13798−13803.

(3) Ravichandran, S.; Nagarajan, S.; Ku, B. C.; Coughlin, B.; Emrick, T.; Kumard, J.; Nagarajan, R. Halogen-Free Ultra-High Flame Retardant Polymers through Enzyme Catalysis. *Green Chem.* **2012**, *14*, 819−824.

(4) Byrne, M. T.; Gun'ko, Y. K. Recent Advances in Research on Carbon Nanotube-Polymer Composites. *Adv. Mater.* **2010**, *22*, 1672−1688.

(5) Shi, Y. M.; Li, L. J. Chemically Modified Graphene: Flame Retardant or Fuel for Combustion? *J. Mater. Chem.* **2011**, *21*, 3277−3279.

(6) Wegner, G.; Wagemann, K. Polymers and the Environment-Current Problems and Future Research. *Adv. Mater.* **1994**, *6*, 629−634.

(7) Kang, N. J.; Wang, D. Y.; Kutlu, B.; Zhao, P. C.; Leuteritz, A.; Wagenknecht, U.; Heinrich, G. A New Approach to Reducing the Flammability of Layered Double Hydroxide (LDH)-Based Polymer Composites: Preparation and Characterization of Dye Structure-Intercalated LDH and Its Effect on the Flammability of Polypropylene-Grafted Maleic Anhydride/d-LDH Composites. *ACS Appl. Mater. Interfaces* **2013**, *5*, 8991−8997.

(8) Pavlidou, S.; Papaspyrides, C. D. A review on polymer-layered silicate nano-composites. *Prog. Polym. Sci.* **2008**, *33*, 1119−1198.

(9) Zhao, B.; Chen, L.; Long, J. W.; Jian, R. K.; Wang, Y. Z. Synergistic Effect between Aluminum Hypophosphite and Alkyl-Substituted Phosphinate in Flame-Retarded Polyamide 6. *Ind. Eng. Chem. Res.* **2013**, *52*, 17162−17170.

(10) Garces, J. M.; Moll, D. J.; Bicerano, J.; Fibiger, R.; McLeod, D. G. Polymeric Nano-composites for Automotive Applications. *Adv. Mater.* **2000**, *12*, 1835−1839.

(11) Fischer, H. Polymer Nanocomposites: From Fundamental Research to Specific Applications. *Mater. Sci. Eng. C* **2003**, *23*, 763−772.
(12) Shen, Z. Q.; Chen, L.; Lin, L.; Deng, C. L.; Zhao, J.; Wang, Y. Z. Synergistic Effect of Layered Nanofillers in Intumescent Flame-Retardant EPDM: Montmorillonite versus Layered Double Hydroxides. *Ind. Eng. Chem. Res.* **2013**, *52*, 8454−8463.
(13) Song, P. A.; Shen, Y.; Du, B. X.; Peng, M.; Shen, L.; Fang, Z. P. Effects of Reactive Compatibilization on the Morphological, Thermal, Mechanical, and Rheological Properties of Intumescent Flame-Retardant Polypropylene. *ACS Appl. Mater. Interfaces* **2009**, *1*, 452−459.
(14) Wang, B. B.; Tang, Q. B.; Hong, N. N.; Song, L.; Wang, L.; Shi, Y. Q.; Hu, Y. Effect of Cellulose Acetate Butyrate Microencapsulated Ammonium Polyphosphate on the Flame Retardancy, Mechanical, Electrical, and Thermal Properties of Intumescent Flame-Retardant Ethylene−Vinyl Acetate Copolymer/Microencapsulated Ammonium Polyphosphate/Polyamide-6 Blends. *ACS Appl. Mater. Interfaces* **2011**, *3*, 3754−3761.
(15) Rothon, R. N.; Hornsby, P. R. Flame Retardant Effects of Magnesium Hydroxide. *Polym. Degrad. Stab.* **1996**, *54*, 383−385.
(16) Pang, H. C.; Ning, G. L.; Gong, W. T.; Ye, J. W.; Lin, Y. Direct Synthesis of Hexagonal $Mg(OH)_2$ Nanoplates from Natural Brucite without Dissolution Procedure. *Chem. Commun.* **2011**, *47*, 6317−6319.
(17) Yu, J. C.; Xu, A. W.; Zhang, L. Z.; Song, R. Q.; Wu, L. Synthesis and Characterization of Porous Magnesium Hydroxide and Oxide Nanoplates. *J. Phys. Chem. B* **2004**, *108*, 64−70.
(18) Minami, H.; Kinoshita, K.; Tsuji, T.; Yanagimoto, H. Preparation of Highly Crystalline Magnesium Oxide and Polystyrene/Magnesium Hydroxide Composite Particles by Sol−Gel Processes in an Ionic Liquid. *J. Phys. Chem. C* **2012**, *116*, 14568−14574.
(19) Gao, Y. H.; Liu, Z. H. Hydrothermal Synthesis and Standard Molar Enthalpy of Formation of Zinc Borate of $4ZnO{\cdot}B_2O_3{\cdot}H_2O$. *J. Chem. Eng. Data* **2009**, *54*, 2789−2790.
(20) Wu, X. F.; Wang, L. C.; Wu, C.; Wang, G. L.; Jian, P. K. Flammability of EVA/IFR (APP/PER/ZB System) and EVA/IFR/Synergist ($CaCO_3$, NG, and EG) Composites. *J. Appl. Polym. Sci.* **2012**, *126*, 1917−1928.
(21) Giorgi, R.; Bozzi, C.; Dei, L.; Gabbiani, C.; Ninham, B. W.; Baglion, P. Nanoparticles of $Mg(OH)_2$: Synthesis and Application to Paper Conservation. *Langmuir* **2005**, *21*, 8495−8501.
(22) Montezin, F.; Lopez-Cuesta, J. M.; Crespy, A.; Georlette, P. Flame Retardant and Mechanical Properties of a Copolymer PP/PE Containing Brominated Compounds/Antimony Trioxide Blends and Magnesium Hydroxide or Talc. *Fire Mater.* **1997**, *21*, 245−252.
(23) Chen, X. L.; Yu, J.; Qin, J.; Luo, Z.; Hu, S. C.; He, M. Combustion Behaviour and Synergistic Effect of Zinc Borate and Microencapsulated Red Phosphorus With Magnesium Hydroxide in Flame-Retarded Polypropylene Composites. *Polym. Polym. Compos.* **2011**, *19*, 491−496.
(24) Durin-France, A.; Ferry, L.; Lopez-Cuesta, J. M.; Crespy, A. Magnesium Hydroxide/Zinc Borate/Talc Compositions as Flame-Retardants in EVA Copolymer. *Polym. Int.* **2000**, *49*, 1101−1105.
(25) Ye, L.; Wu, Q. H.; Qu, B. J. Synergistic Effects and Mechanism of Multiwalled Carbon Nanotubes with Magnesium Hydroxide in Halogen-Free Flame Retardant EVA/MH/MWNT Nanocomposites. *Polym. Degrad. Stab.* **2009**, *94*, 751−756.
(26) Hornsby, P. R.; Cusack, P. A.; Cross, M.; Toth, A.; Zelei, B.; Marosi, G. ZHS-coated Metal Hydroxide Flame Retardants: Fire Performance and Substrate Coating Interation. *J. Mater. Sci.* **2003**, *38*, 2893−2899.
(27) Li, X.; Ye, J. W.; Lin, Y.; Fan, L. L.; Ning, G. L. Synergistic Flame Retarded Effect of Synthetic Dawsonite on EVA/Magnesium Hydroxide System. *Polym.−Plast. Technol. Eng.* **2010**, *49*, 861−886.
(28) Cross, M. S.; Cusack, P. A.; Hornsby, P. R. Effects of Tin Additives on the Flammability and Smoke Emission Characteristics of Halogen-Free Ethylene-Vinyl Acetate Copolymer. *Polym. Degrad. Stab.* **2003**, *79*, 309−318.
(29) Wang, Z. Z.; Qu, B. J.; Fan, W. C.; Huang, P. Combustion Characteristics of Halogen-Free Flame-Retarded Polyethylene Containing Magnesium Hydroxide and Some Synergists. *J. Appl. Polym. Sci.* **2001**, *81*, 206−214.
(30) Carpentier, F.; Bourbigot, S.; Bras, M. L.; Delobel, R.; Foulon, M. Charring of Fire Retarded Ethylene Vinyl Acetate Copolymer-Magnesium Hydroxide/Zinc Borate Formulations. *Polym. Degrad. Stab.* **2000**, *69*, 83−92.
(31) Xie, R. C.; Qu, B. J. Expandable graphite systems for halogen-free flame-retarding of polyolefins. I. Flammability characterization and synergistic effect. *J. Appl. Polym. Sci.* **2001**, *80*, 1181−1189.
(32) Fu, M. Z.; Qu, B. J. Synergistic Flame Retardant Mechanism of Fumed Silica in Ethylene-Vinyl Acetate/Magnesium Hydroxide Blends. *Polym. Degrad. Stab.* **2004**, *85*, 633−639.
(33) Carpentier, F.; Bourbigot, S.; Bras, M. L.; Delobel, R. Rheological Investigations in Fire Retardancy: Application to Ethylene-Vinyl-Acetate Copolymer-Magnesium Hydroxide/Zinc Borate Formulations. *Polym. Int.* **2000**, *49*, 1216−1221.
(34) Bourbigot, S.; Carpentier, F.; Bras, M. L. Thermal Degradation and Combustion Mechanism of EVA-Magnesium Hydroxide-Zinc Borate. *Fire and Polymers* **2001**, *14*, 173−185.
(35) Liu, S.P.; Ying, J. R.; Zhou, X. P.; Xie, X. L.; Mai, Y. W. Dispersion, Thermal and Mechanical Properties of Polypropylene/Magnesium Hydroxide Nanocomposites Compatibilized by SEBS-g-MA. *Compos. Sci. Technol.* **2009**, *69*, 1873−1879.
(36) Shen, K. K. Zinc Borates: 30 Years of Successful Development as Multifunctional Fire Retardants. *Fire and Polymers* **2001**, *18*, 228−239.
(37) Bourbigot, S.; Bras, M. L.; Leeuwendal, R.; Shen, K. K.; Schubert, D. Recent Advances in the Use of Zinc Borates in Flame Retardancy of EVA. *Polym. Degrad. Stab.* **1999**, *64*, 419−425.
(38) Schubert, D. M.; Alam, F.; Visi, M. Z.; Knobler, C. B. Structural Characterization and Chemistry of the Industrially Important Zinc Borate, $Zn[B_3O_4(OH)_3]$. *Chem. Mater.* **2003**, *15*, 866−871.
(39) Wu, Z. P.; Hu, Y. C.; Shu, W. G. Influence of Ultrafine Zinc Borate on the Thermal Degradation Behavior of a (Low-Density Polyethylene)/(Intumescent Flame Retardant) System. *J. Vinyl Addit. Technol.* **2009**, *15*, 260−265.
(40) Shen, K. K.; Griffin, T. S. Zinc Borate as a Flame Retardant, Smoke Suppressant, and Afterglow Suppressant in Polymers. *Fire Polym.* **1990**, *12*, 157−177.
(41) Wang, X. S.; Pang, H. C.; Chen, W. D.; Lin, Y.; Ning, G. L. Nanoengineering Core/Shell Structured Brucite@Polyphosphate@Amine Hybrid System for Enhanced Flame Retardant Properties. *Polym. Degrad. Stab.* **2013**, *98*, 2609−2616.
(42) Wang, H. Y.; Ye, J. W.; Zhou, Y. R.; Gong, W. T.; Lin, Y.; Ning, G. L. Preparation and Characterization of Low Hydrated Zinc Borate $Zn_6O(OH)(BO_3)_3$. *Chin. J. Inorg. Chem. Ind.* **2012**, *44*, 19−21.
(43) Leonard, J. E.; Bowditch, P. A.; Dowling, V. P. Development of a Controlled-Atmosphere Cone Calorimeter. *Fire Mater.* **2000**, *24*, 143−150.
(44) Schartel, B.; Hull, T. R. Development of Fire-Retardant Materials—Interpretation of Cone Calorimeter Data. *Fire Mater.* **2007**, *31*, 327−354.
(45) Harrison, W. T. A.; Gier, T. E.; Stucky, G. D. The Synthesis and Ab Initio Structure Determination of $Zn_4O(BO_3)_2$ a Microporous, Zincoborate Constructed of "Fused" Subunits, of Three- and Five-Membered Rings. *Angew. Chem., Int. Ed. Engl.* **1993**, *32*, 724−726.
(46) Delahaye, T.; Boucher, F.; Paris, M.; Joubert, O.; Caldes, M.; Piffard, Y. Some Experimental Evidence That $Zn_4O(BO_3)_2$ is $Zn_6O(OH)(BO_3)_3$. *Angew. Chem., Int. Ed.* **2006**, *45*, 4060−4062.
(47) Wang, J.; Tung, J. F.; Fuad, M. Y. A.; Hornsby, P. R. Microstructure and Mechanical Properties of Ternary Phase Polypropylene/Elastomer/Magnesium Hydroxide Fire-Retardant Compositions. *J. Appl. Polym. Sci.* **1996**, *60*, 1425−1437.
(48) Jeziórska, R.; Świerz-Motysia, B.; Zielecka, M.; Szadkowska, A.; Studziński, M. Structure and Mechanical Properties of Low-Density Polyethylene/Spherical Silica Nanocomposites Prepared by Melt

Mixing: The Joint Action of Silica's Size, Functionality, and Compatibilizer. *J. Appl. Polym. Sci.* **2012**, *125*, 4326−4337.
(49) Osman, M. A.; Atallah, A. Effect of the Particle Size on the Viscoelastic Properties of Filled Polyethylene. *Polymer* **2006**, *47*, 2357−2368.
(50) Osman, M. A.; Atallah, A. Interparticle and Particle−Matrix Interactions in Polyethylene Reinforcement and Viscoelasticity. *Polymer* **2005**, *46*, 9476−9488.
(51) Luo, M. C.; Liao, X. X.; Liao, S. Q.; Zhao, Y. F. Mechanical and Dynamic Mechanical Properties of Natural Rubber Blended with Waste Rubber Powder Modified by Both Microwave and Sol−Gel Method. *J. Appl. Polym. Sci.* **2013**, *129*, 2313−2320.
(52) Isitman, N. A.; Gunduz, H. O.; Kaynak, C. Nanoclay Synergy in Flame Retarded/Glass Fibre Reinforced Polyamide 6. *Polym. Degrad. Stab.* **2009**, *94*, 2241−2250.
(53) Wang, X. S.; Pang, H. C.; Chen, W. D.; Lin, Y.; Ning, G. L. Controllable Fabrication of High Purity $Mg(OH)_2$ Nanoneedles via Direct Transformation of Natural Brucite. *Mater. Lett.* **2014**, *120*, 69−72.
(54) Balakrishnan, H.; Hassan, A.; Isitman, N. A.; Kaynak, C. On the use of Magnesium Hydroxide Towards Halogen-Free Flame-Retarded Polyamide-6/Polypropylene Blends. *Polym. Degrad. Stab.* **2012**, *97*, 1447−1457.
(55) McKee, D. W. Borate treatment of carbon fibers and carbon/carbon composites for improved oxidation resistance. *Carbon* **1986**, *24*, 737−741.
(56) Hirschler, M. M.; Thevaranjan, T. R. Effects of Magnesium Oxide/Hydroxide on Flammability and Smoke Production Tendency of Polystyrene. *Eur. Polym. J.* **1985**, *21*, 371−375.
(57) Fei, G.; Liu, Y.; Wang, Q. Synergistic Effects of Novolac-Based Char Former with Magnesium Hydroxide in Flame Retardant Polyamide-6. *Polym. Degrad. Stab.* **2008**, *93*, 1351−1356.
(58) Laufer, G.; Kirkland, C.; Cain, A. A.; Grunlan, J. C. Clay−Chitosan Nanobrick Walls: Completely Renewable Gas Barrier and Flame-Retardant Nanocoatings. *ACS Appl. Mater. Interfaces* **2012**, *4*, 1643−1649.